Nonlinear evolution of an interface in the Richtmyer-Meshkov instability

Chihiro Matsuoka*

Department of Physics, Ehime University, 2-5, Bunkyocho, Matsuyama, Ehime 790-8577, Japan

Katsunobu Nishihara† and Yuko Fukuda

Institute of Laser Engineering, Osaka University, 2-6, Yamada-oka Suita, Osaka 565-0871, Japan

The linear theory of the Richtmyer-Meshkov instability derived by Wouchuk and Nishihara [Phys. Plasmas **4**, 3761 (1997)] indicates that the instability is driven by the nonuniform velocity shear left by transmitted and reflected rippled shocks at a corrugated interface. In this work, the nonlinear evolution of the interface has been investigated as a self-interaction of a nonuniform vortex sheet with a density jump. The theory developed shows the importance of the finite density jump and the finite initial corrugation amplitude of the interface. By introducing Lagrangian markers on the interface with proper kinematic boundary conditions, it is shown that stretching and shrinking of the interface occur locally even in the tangential direction. This causes deformation of bubble and spike profiles depending on the Atwood number. The vorticity on the interface for a finite density jump is not conserved in the nonlinear regime. Our results suggest that the spiral structure of the spike is due to local increase and decrease of the vorticity on the interface. Nonlinear analysis shows that the large initial amplitude of the corrugation results in rapid increase of the vorticity, which may also explain the fast roll up motion of the spiral for large amplitudes. With the use of the asymptotic linear growth rate, the nonlinear evolution of the instability is uniquely determined from the initial corrugation amplitude of the interface, the Atwood number, and the incident shock intensity. There is no need to use an impulsive formulation. The analytical nonlinear growth agrees well with the experiment [Dimonte *et al.*, Phys. Plasmas **3**, 614 (1996)]. The theory reveals nonlinear properties of the instability, such as the time evolution of the interface profiles and the vorticity on the interface, and also their dependence on the Atwood number and the corrugation amplitude.

I. INTRODUCTION

When a shock wave passes through a corrugated interface between two fluids with different densities, the perturbed interface is deformed and eventually rolls up like a mushroom. This phenomenon is known as the Richtmyer-Meshkov (RM) instability [1–5], and the interface perturbation grows linearly with respect to time t in the linear regime. The RM instability is of direct importance in inertial confinement fusion any time a shock wave crosses layers of materials with different densities.

A lot of researchers including Richtmyer have tried to explain this instability with an impulsive gravitational acceleration term. However, Wouchuk and Nishihara formula for the RM growth rate [6,7] indicates that the RM instability essentially grows due to vorticity left by transmitted and reflected rippled shocks (or reflected rarefaction) at the corrugated interface. This is also confirmed from our simulations in this paper. The vorticity may not be uniformly distributed along the interface when the incident shock passes through the corrugated surface, which leads to local stretching and shrinking of the interface. As will be shown below, when the density jump is finite across the interface, the stretching and shrinking of the interface occur even in the tangential direction. This causes different profiles for bubble and spike depending on the Atwood number. In linear theory, after the instability reaches the asymptotic linear growth rate, the vor-

ticity on the interface does not change with time. However, the vorticity is not conserved in the nonlinear regime for a finite density jump. A spiral structure of the spike appears in the strongly nonlinear regime of the instability [3]. Nonlinear increase of the vorticity may cause formation of the spiral. Therefore, we need a nonlinear model so that we can describe the nonlinear evolution of both the interface profile and vorticity on the interface self-consistently with the density jump.

When the incident shock is strong, the bulk vorticity generated behind the transmitted shock cannot be ignored. Nevertheless, when the shock is weak, the linear RM instability grows only due to the vorticity that the shocks left at the interface [6–8]. This indicates that the nonlinear evolution of the RM instability can be treated as a vortex sheet with a spatial inhomogeneity.

Regarding the initial disturbance, we can classify the Rayleigh-Taylor (RT) instability, the Kelvin-Helmholtz (KH) instability, and the RM instability as follows.

(1) There exists no vorticity on the interface at $t=0$ in the RT instability.

(2) A homogeneous (one-dimensional) strong vorticity distributes on the interface at $t=0$ in the KH instability.

(3) There exists an inhomogeneous (two-dimensional) weak vorticity on the interface in the RM instability.

The inhomogeneous vorticity distribution in the RM instability comes from the fact that the initial interface is oblique to the incident shock. In Ref. [9], the interface growth in the RT and RM instabilities is explained from the vortex viewpoint: Zabusky solved numerically a vorticity equation derived from a compressible Euler equation and investigated

---
*Electronic address: matsuoka@phys.sci.ehime-u.ac.jp

†Electronic address: nishihara@ile.osaka-u.ac.jp

the bubble and spike structures together with their growth rates in detail. There are also some works in which the interface is treated as a vortex sheet [10], the sheet is split into point vortices and the temporal evolution of the interface is investigated numerically. However, following two points cannot be explained with their point vortex model, the stretching or shrinking of the sheet described above and temporal evolution of circulation due to the finite Atwood number in this system. There are some other approaches investigating the temporal evolution and growth rate of the interface with a weakly nonlinear analysis [11,12]. Their weakly nonlinear analysis, however, assumes that the interface moves only to the normal direction in spite of the fact that the interface also expands and contracts in the tangential direction.

In this paper, we parametrize the interface with Lagrangian markers. We then show that for nonuniform vorticity on the interface with a finite density jump, the interface expands and contracts even in the tangential direction. We also present proper kinematic boundary conditions in order to describe the nonlinear evolution of the interface with the temporal evolution of the circulation on the interface. Comparison of analytical results with simulations indicates that local increase and decrease of the vorticity cause formation of the spiral structure in the strongly nonlinear regime of the instability. Nonlinear analysis also shows that the increase of the vorticity depends strongly on the initial corrugation amplitude, which may explain simulation results [13] that the large corrugation amplitude leads to fast roll up motion of the spiral.

Here we do not adopt the impulsive gravitational acceleration derived phenomenologically by Richtmyer, since the velocity shear at the interface is not uniquely determined only from the impulsive acceleration, which causes the failure of the impulsive model. Instead, the asymptotic linear growth rate derived in Ref. [7] is used to initialize the nonlinear model. As a matter of fact, the use of the linear growth rate derived in Ref. [7] is restricted to low Mach numbers of the incident shock. In this way, the generation of vorticity in fluids can be neglected. Roughly speaking, shock Mach number should be less than 2. However, there could be situations in which fair agreement with simulations or experiments can be found at a higher Mach number. We also assume that fluids are incompressible, which is verified independently to shock Mach number in an asymptotic stage of the linear growth [6]. Initial amplitudes of the interface corrugation are assumed to be finite but small compared with its wavelength. Because of Taylor series expansion employed in the analytical calculation, the mushroom structure of the spike cannot be resolved.

In Sec. II, we show that the nonlinear evolution of the RM instability can be described as a self-interaction of a nonuniform vortex sheet by comparing its nonlinear dynamics with that of a shocked interface with the use of two-dimensional hydrodynamic simulations. In Sec. III, we develop a nonlinear theory that describes the nonlinear evolution of the nonuniform vortex sheet with the density jump across it. In Sec. IV, we show results of the nonlinear growth rate and profiles of bubble and spike, and the nonlinear evolution of the cir-

culation on the vortex sheet comparing with simulations and previous works. We also discuss the dependence of these properties of the RM instability on the Atwood number and on the initial corrugation amplitude. We summarize our work in Sec. V.

II. SHOCKED INTERFACE AND NONUNIFORM VORTEX SHEET

As mentioned in the Introduction, the RM instability occurs due to the vorticity left behind the rippled shocks after the incident shock passes through a corrugated interface. This indicates that nonlinear dynamics of the unstable interface can be treated as a self-interaction of a nonuniform vortex sheet with a density jump. With the use of two-dimensional hydrodynamic code IMPACT2D [14], we have compared two cases; one is the case in which an incident shock hits a sinusoidal interface between two different fluids from a light fluid to a heavy fluid, and the other is the case that the velocity shear is initially imposed on the sinusoidal interface without the incident shock.

We suppose that at $y=0$ there is an interface that separates two fluids: light fluid "1" ($y>0$) and heavy fluid "2" ($y<0$). A shock propagating through the light fluid with velocity u_i (<0) hits the interface at $t=0$. The fluid velocity behind the incident shock is v_1 (<0) for $t<0$. At $t=0+$, the shock is transmitted into fluid 2 that moves with velocity u_t (<0) and the density behind the transmitted shock is ρ_2. On the other hand, in fluid 1 another shock is reflected. In this paper, we consider only the case of the reflected shock, but the results are the same for a reflected rarefaction. The reflected shock velocity and the density behind the reflected shock are u_r (>0) and ρ_1, respectively. As a result of the shock-interface interaction, the interface moves with velocity v_i (<0).

In the latter case, i.e., the velocity shear on the sinusoidal interface without the incident shock, we have used following initial conditions with knowledge of the asymptotic linear growth rate of the RM instability [7]. With the assumption that in the asymptotic stage both fluids become incompressible and irrotational, the theory shows that the asymptotic linear growth rate is given by

$$v_{lin} = \frac{\rho_1 \delta v_{1x+} - \rho_2 \delta v_{2x+}}{\rho_1 + \rho_2}, \qquad (1)$$

where δv_{1x+} and δv_{2x+} are tangential velocity perturbations behind the reflected and transmitted shocks at $t=0+$, respectively. They are uniquely determined from the initial amplitude of the corrugation and the incident shock intensity. Let us assume that the interface has an initial corrugation of a form $y = \hat{\alpha}_0 \cos(kx)$, where $\hat{\alpha}_0$ is a corrugation amplitude before the shock hits the interface, $k = 2\pi/\lambda$ is the perturbation wave number and λ is the wavelength. If the initial amplitude is very small compared with the wavelength, the ripple amplitudes of the transmitted and reflected shock fronts are, respectively, approximated as,

$$\hat{\alpha}_t = \hat{\alpha}_0 (1 - u_t/u_i), \quad \hat{\alpha}_r = \hat{\alpha}_0 (1 - u_r/u_i). \qquad (2)$$

TABLE I. Simulation parameters: ρ_1, light fluid mass density; ρ_2, heavy fluid mass density; p, pressure at interface; $\hat{\alpha}$, initial corrugation amplitude; and v_{lin}, initial velocity shear.

	Shocked interface	Vortex sheet
ρ_1 (g/cm^3)	4×10^{-2}	1.0677×10^{-1}
ρ_2 (g/cm^3)	9.3333×10^{-2}	2.3549×10^{-1}
p (Mbar)	1	6.1567
$\hat{\alpha}$ (μm)	4.6322	2.56
v_{lin} (cm/sec)		3.6465×10^5

The shock front ripples lead to the tangential velocity at both sides of the interface at $t = 0+$ as

$$\delta v_{1x+} = k \hat{\alpha}_r (v_i - v_1), \quad \delta v_{2x+} = k \hat{\alpha}_t v_i. \qquad (3)$$

In general, both values are different and an initial vorticity $\kappa = \delta v_{1x+} - \delta v_{2x+}$ exists at the interface. If a rarefaction is reflected instead of a shock, then the shear velocity δv_{1x+} should be calculated as in Ref. [15]. Later on, as the shocks separate away, the initial vorticity will change due to baroclinic generation of the vorticity caused by pressure perturbations behind the shocks and the density jump across the interface. In the bulk, however, first-order vorticity is only generated at the shock fronts. In Ref. [7], it was proved that pressure and density perturbations between the shocks vanish when the shocks are sufficiently far away. This is independent of the incident shock strength. This means that the perturbed velocity field asymptotically becomes incompressible. It was also shown in Ref. [6] that the bulk vorticity is of second order in the shock intensity for a weak shock. Therefore, in the weak shock limit, we have the following relations among the amplitudes of the asymptotic velocity perturbations at the interface, $\delta v_{lin} = \delta v_{1x} = -\delta v_{2x}$.

Thus by introducing the velocity potentials in both fluids and the corrugation amplitude of the interface as

$$\phi = \mp \frac{v_{lin}}{k} \exp[\mp k(y - \hat{\alpha}\cos kx)]\cos kx \quad \text{for} \quad y \gtrless \hat{\alpha},$$

$$\hat{\alpha} = \hat{\alpha}_0 (1 - v_i / u_i), \qquad (4)$$

respectively, we can give the initial velocity shear on the corrugated interface. The corrugation amplitude of the interface in the case of the vortex sheet, $\hat{\alpha}$, should coincide with the one at $t = 0+$ in the case that the incident shock passes through it.

In the simulations, we used an ideal gas equation of state with adiabatic exponent 5/3 for both fluids. The incident shock Mach number is 2 and the wavelength of the sinusoidal corrugation is 128 μm. The other parameters are shown in Table I. Note that all of the parameters for the vortex sheet correspond to the postshock condition and they are calculated from the shock jump conditions and Eq. (4).

Figure 1 shows density profiles of two cases with gray scale. Hereafter, we show simulation results in a frame moving with the velocity of the undisturbed interface after the
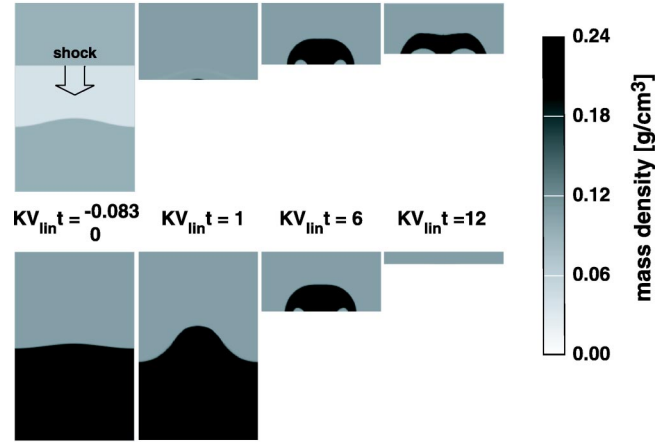
FIG. 1. Density profiles for the case in which a shock hits an interface (top), and for the case in which velocity shear is initially imposed on the corrugated interface without shock incident (bottom) at different times. Gray scale shows fluid mass density (g/cm^3).

incident shock passes through it, i.e., v_i. Top four are the cases of the shocked interface at normalized time of $kv_{lin}t = -0.083$, 1, 6, and 12 from left to right. The incident shock hits the corrugation surface at normalized time $kv_{lin}t = 0$. Bottom four are the cases of the vortex sheet at normalized time of $kv_{lin}t = 0$, 1, 6, and 12 from left to right. The initial Atwood number and corrugation amplitude of the interface are 0.4 and $\hat{\alpha}_0/\lambda = 0.0362$ for the shocked interface and those are $A \cong 0.376$ and $\hat{\alpha}/\lambda \cong 0.02$ for the vortex sheet, respectively (see Table I). The results show that profiles of bubble and spike, even mushroom and spiral structures of the spike, are almost the same for both cases, except noticeable difference of the bubble structure and the thickness of the spike. The difference may be due to the facts that the bulk vorticity behind the transmitted shock suppresses the growth of the bubble and also that during the interaction of the incident shock with the corrugated interface, higher harmonics of the corrugation and the velocity shear may arise at the interface in the case of the shocked interface.

Nonlinear evolution of the interface is tracked using the Lagrangian markers on the interface within second order of accuracy in both time and space. Figure 2 shows time dependence of the nonlinear growth rates normalized by the asymptotic linear growth rate v_{lin} given by Eq. (1) for two cases. The positive and negative values correspond to the spike and bubble growth rates, respectively. Dashed and dotted line and thin solid line with closed circles indicate the growth rate for the shocked interface and that for the vortex sheet, respectively. They agree fairly well with each other except in early time due to the finite transition time required for the incident shock to pass through the interface with the finite corrugation amplitude and also that required for the instability to reach the asymptotic linear growth rate. The oscillation of the growth rate for the shocked case is due to the fact that the sound waves propagate back and forth between the reflected and transmitted shocks. In the linear re-
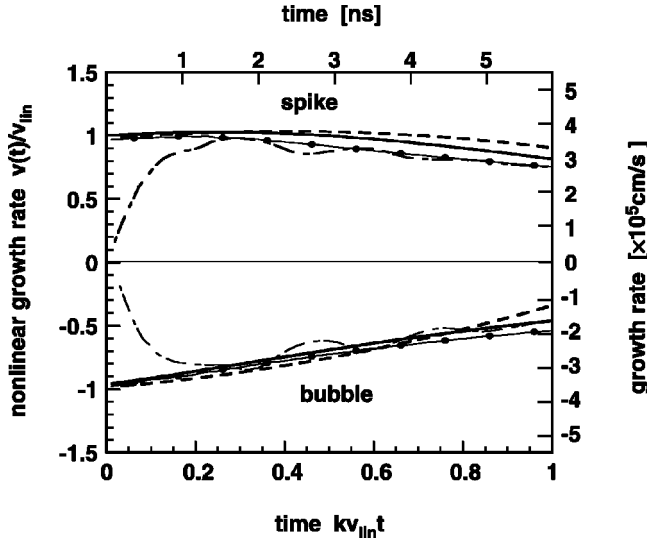
FIG. 2. Nonlinear growth rate of bubble (bottom) and spike (top) normalized by the asymptotic linear growth rate v_{lin} as a function of normalized time, $\tau = k v_{lin} t$. Their dimensional values are also shown in the left and top scales. Dashed and dotted lines and thin solid lines with closed circles depict the simulation results for the cases in which the incident shock hits a corrugated interface and a nonuniform velocity shear exists at $\tau = 0$ on the interface, respectively, while thick solid and dashed lines depict the result from the third-order nonlinear analysis for the cases with and without the Padé approximants P_2^0, respectively.

gime, the growth rates of the bubble and spike are the same. However, they are not the same in the nonlinear regime as shown in the figure. The growth rate of the spike is larger than that of the bubble in the nonlinear regime. The nonlinear growth of the spike increases from its initial value and reaches its maximum value around time of $k v_{lin} t = 0.2$ in the case of the vortex sheet and $k v_{lin} t = 0.3$ in the case of the shocked interface, and then decays slowly compared with that of the bubble. As clearly seen from the figure, the nonlinear growth rate of the bubble decays faster than that of the spike in both cases.

The above agreement between both cases indicates that the RM instability grows due to the nonuniform velocity shear that the transmitted and reflected shocks leave at the corrugated interface. We would like to mention that the use of the linear asymptotic growth rate for the initial velocity shear gives not only qualitative agreement but also quantitative agreement in both cases. It should also be noted that the asymptotic linear growth rate is uniquely determined from the incident shock intensity, the Atwood number, adiabatic coefficients, and the initial corrugation amplitude.

III. NONLINEAR ANALYSIS FOR BASIC EQUATIONS

A. Derivation of the basic equations

We consider the self-interaction of a nonuniform vortex sheet with a density jump. The fluids have different densities, and therefore, the circulation in this system is not conserved due to the baroclinic effect. When surface tension and gravi-

tational acceleration are neglected, the temporal evolution of the circulation Γ on the interface is given by the following equation:

$$\frac{D\Gamma}{Dt} = 2A \left[\frac{D\Phi}{Dt} - \frac{1}{2} \boldsymbol{q} \cdot \boldsymbol{q} - \frac{1}{8} \boldsymbol{\kappa} \cdot \boldsymbol{\kappa} + \frac{A}{2} \boldsymbol{\kappa} \cdot \boldsymbol{q} \right]_{\text{interface}}, \quad (5)$$

$$\frac{D}{Dt} = \frac{\partial}{\partial t} + \bar{\boldsymbol{u}} \cdot \nabla, \quad \bar{\boldsymbol{u}} \equiv \frac{\rho_1 \boldsymbol{u}_1 + \rho_2 \boldsymbol{u}_2}{\rho_1 + \rho_2} = \boldsymbol{q} - \frac{A\boldsymbol{\kappa}}{2}, \quad (6)$$

where $\boldsymbol{\kappa} = \boldsymbol{u}_1 - \boldsymbol{u}_2$ is the vorticity induced on the sheet and $\boldsymbol{q} = (\boldsymbol{u}_1 + \boldsymbol{u}_2)/2$ is an average of the velocities on the two sides with the velocity $\boldsymbol{u}_i (i=1,2)$ in each side and $\Phi = (\phi_1 + \phi_2)/2$ is the average velocity potential related with $\boldsymbol{u}_i = \nabla \phi_i$. The circulation $\Gamma = \phi_1 - \phi_2$ is also related to $\boldsymbol{\kappa}$ as $\boldsymbol{\kappa} = \nabla \Gamma$. The fluid particle on the interface is set so that they move with velocity $\bar{\boldsymbol{u}}$ in Eq. (6), which assures that Eq. (5) is equivalent to the Bernoulli equation, i.e., the pressure continuous condition across the interface. Equation (5) is derived by integrating the Euler equation along the interface. For the detailed derivation of Eq. (5), refer to the Appendix. Similar equation was derived by Baker *et al.* using the complex velocity potential [16]. As we can easily see from Eq. (5), the circulation Γ is not a conserved quantity if $A \neq 0$. From now on, we consider the two-dimensional case, although Eqs. (5) and (6) also hold in the three-dimensional case.

The system is assumed to be incompressible, therefore, the velocity potential satisfies the Laplace equation in each region:

$$\triangle \phi_i = 0 \quad (i=1,2). \quad (7)$$

We now consider the interface as a curve in the (x,y) plane, and parametrize it using a parameter Θ, the Lagrangian marker,

$$x = \Theta + X(\Theta, t),$$
$$y = Y(\Theta, t), \quad (8)$$

where y denotes the vertical coordinate. We set $x = \Theta$ at $t = 0$. Then the unit normal vector $\boldsymbol{n}$ and the unit tangential vector $\boldsymbol{t}$ to the interface are given by following expressions:

$$\boldsymbol{n} = \frac{(-Y_\Theta, 1+X_\Theta)}{\sqrt{(1+X_\Theta)^2 + Y_\Theta^2}}, \quad \boldsymbol{t} = \frac{(1+X_\Theta, Y_\Theta)}{\sqrt{(1+X_\Theta)^2 + Y_\Theta^2}}, \quad (9)$$

where the subscript denotes the differentiation with respect to the variable. Note that Eq. (8) admits multivalued solutions like a spiral because we do not assume that y can be solved as a function of the variable x, $y = Y(x;t)$.

The kinematic boundary conditions at the interface are then given as

$$\boldsymbol{r}_t \cdot \boldsymbol{n} = \bar{\boldsymbol{u}} \cdot \boldsymbol{n} = \frac{\rho_1 \nabla \phi_1 \cdot \boldsymbol{n} + \rho_2 \nabla \phi_2 \cdot \boldsymbol{n}}{\rho_1 + \rho_2} \Big|_{\text{interface}}, \quad (10)$$
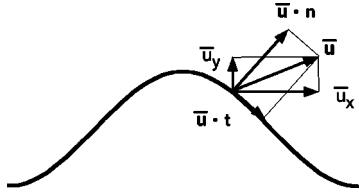
FIG. 3. Schematic picture of kinematic boundary conditions, where $\bar{\boldsymbol{u}} = (\bar{u}_x, \bar{u}_y)$ denote interface velocity. Note that $\bar{\boldsymbol{u}}$ is not in the normal direction to the interface.

$$\boldsymbol{r}_t \cdot \boldsymbol{t} = \bar{\boldsymbol{u}} \cdot \boldsymbol{t} = \frac{\rho_1 \nabla \phi_1 \cdot \boldsymbol{t} + \rho_2 \nabla \phi_2 \cdot \boldsymbol{t}}{\rho_1 + \rho_2} \Big|_{\text{interface}} \quad (11)$$

with the continuity condition of the normal velocity at the interface

$$\nabla \phi_1 \cdot \boldsymbol{n} = \nabla \phi_2 \cdot \boldsymbol{n}, \quad (12)$$

where $\boldsymbol{r}_t$ is given by (X_t, Y_t). It should be mentioned that the interface motion satisfies the continuity condition of the normal velocity, $\bar{\boldsymbol{u}} \cdot \boldsymbol{n} = \boldsymbol{u}_1 \cdot \boldsymbol{n} = \boldsymbol{u}_2 \cdot \boldsymbol{n}$.

Note also that Eq. (11) does not indicate that the tangential velocities of both fluids are continuous at the interface. The tangential velocity of the interface is arbitrarily determined and is here given as the velocity of the fluid particle on the interface obtained from projecting $\bar{\boldsymbol{u}}$ in Eq. (6) into the tangential direction. This condition is set taking into account that the initial disturbance is two dimensional, which enables us to describe the stretching and shrinking of the interface. Equations (10)–(12) with Eq. (5) are the boundary conditions required to determine the nonlinear evolution of the interface.

We discuss here the difference between the kinematic boundary condition used in the analysis of the KH instability and that of the RM instability. If we can ignore the stretching and shrinking in the tangential direction as in the case of the KH instability, we can express the profile of the interface as a function of x; $y = Y(x,t)$. Then, instead of Eq. (10) with Eq. (12), the kinematic boundary condition becomes as follows:

$$\frac{\partial Y}{\partial t} = \frac{\partial \phi_i}{\partial y} - \frac{\partial Y}{\partial x}\frac{\partial \phi_i}{\partial x} \quad (i=1,2), \quad (13)$$

which is obtained by substituting

$$\boldsymbol{n} = \frac{(-Y_x, 1)}{\sqrt{1 + Y_x^2}}, \quad \boldsymbol{r}_t = (0, Y_t)$$

into Eq. (10) and taking Eq. (12) into account. This condition was adopted in the previous works by Velikovich and Dimonte (Eq. (2) in Ref. [11]) and Zhang et al.(Eqs. (3) and (4) in Ref. [12]). However, it is not adequate to follow the temporal evolution of the stretched interface as found in the RM instability. We show the boundary conditions given by Eqs. (10) and (11) schematically in Fig. 3.

B. Solution to the basic equations

The normalized initial amplitude of the interface corrugation, $\hat{a}/\lambda$, is assumed to be small so that we can formally expand X and Y in Eq. (8) with a small parameter ϵ as

$$X = \epsilon X^{(1)} + \epsilon^2 X^{(2)} + \cdots,$$

$$Y = \epsilon Y^{(1)} + \epsilon^2 Y^{(2)} + \cdots,$$

and the velocity potential ϕ_i ($i=1,2$) can also be expanded as

$$\phi_1 = \sum_{n=1}^{\infty} \epsilon^n \phi_1^{(n)} = \sum_{n=1}^{\infty} \epsilon^n B_1^{(n)}(t) e^{-nky} \cos nkx \quad (y>0),$$

$$\phi_2 = \sum_{n=1}^{\infty} \epsilon^n \phi_2^{(n)} = \sum_{n=1}^{\infty} \epsilon^n B_2^{(n)}(t) e^{nky} \cos nkx \quad (y<0),$$

(14)

where $B_i^{(n)}(t)$ is the amplitude of the nth mode $\phi_i^{(n)}$. In order to evaluate the boundary condition at $x = \Theta$ and $y = 0$ instead of $x = \Theta + X(\Theta)$ and $y = Y(\Theta)$, we expand ϕ_i in the Taylor series at $x = \Theta$ and $y = 0$ as

$$\begin{aligned}
\phi_i|_{\text{interface}} &= \phi_i\big|_0 + \frac{\partial \phi_i}{\partial x}\Big|_0 X + \frac{\partial \phi_i}{\partial y}\Big|_0 Y \\
&+ \frac{1}{2}\left(\frac{\partial^2 \phi_i}{\partial x^2}\Big|_0 X^2 + \frac{\partial^2 \phi_i}{\partial y^2}\Big|_0 Y^2 \right) + \frac{\partial^2 \phi_i}{\partial x \partial y}\Big|_0 XY \\
&+ \frac{1}{6}\left(\frac{\partial^3 \phi_i}{\partial x^3}\Big|_0 X^3 + \frac{\partial^3 \phi_i}{\partial y^3}\Big|_0 Y^3 \right) \\
&+ \frac{1}{2}\left(\frac{\partial^3 \phi_i}{\partial x^2 \partial y}\Big|_0 X^2 Y + \frac{\partial^3 \phi_i}{\partial x \partial y^2}\Big|_0 XY^2 \right) + \cdots,
\end{aligned}$$

(15)

from which we obtain

$$\frac{\partial \phi_i^{(1)}}{\partial x}\Big|_{\text{interface}} = \frac{\partial \phi_i^{(1)}}{\partial x}\Big|_0,$$

$$\frac{\partial \phi_i^{(2)}}{\partial x}\Big|_{\text{interface}} = \frac{\partial \phi_i^{(1)}}{\partial x}\Big|_0 X^{(1)} + \frac{\partial \phi_i^{(1)}}{\partial y}\Big|_0 Y^{(1)}, \frac{\partial \phi_i^{(3)}}{\partial x}\Big|_{\text{interface}}$$

$$= \frac{\partial \phi_i^{(3)}}{\partial x}\Big|_0 + \frac{\partial \phi_i^{(2)}}{\partial x}\Big|_0 X^{(1)} + \frac{\partial \phi_i^{(2)}}{\partial y}\Big|_0 Y^{(1)}$$

$$+ \frac{\partial \phi_i^{(1)}}{\partial x}\Big|_0 X^{(2)} + \frac{\partial \phi_i^{(1)}}{\partial y}\Big|_0 Y^{(2)}$$

$$+ \frac{1}{2}\left(\frac{\partial^2 \phi_i^{(1)}}{\partial x^2}\Big|_0 (X^{(1)})^2 + \frac{\partial^2 \phi_i^{(1)}}{\partial y^2}\Big|_0 (Y^{(1)})^2 \right)$$

$$+ \frac{\partial^2 \phi_i^{(1)}}{\partial x \partial y}\Big|_0 X^{(1)} Y^{(1)} + \cdots$$

and so on. Here the subscript 0 indicates that the value of the function is taken at $x = \Theta$ and $y = 0$.

From now on we introduce the dimensionless variables $\xi = kX$, $\eta = kY$, $\theta = k\Theta$, $\tau = k^2 B_1 t = k v_{lin} t$ and $\tilde{\phi}_i = \phi_i / B_1$, and describe all quantities by using them, where $k B_1 \equiv v_{lin} = -k B_1^{(1)}(0) = k B_2^{(1)}(0)$ is the asymptotic linear growth rate given by Eq. (1).

Taking into account the form of $\boldsymbol{n}$ and $\boldsymbol{t}$ in Eq. (9), and substituting into Eqs. (5), (10)–(12), we have at first order;

$$\xi^{(1)} = -A\tau \sin\theta,$$

$$\eta^{(1)} = (\alpha + \tau)\cos\theta, \tag{16}$$

where α is the dimensionless initial amplitude of the interface, i.e., $\alpha = 2\pi\hat{a}/\lambda$. It should be noted that the Lagrangian marker on the interface moves with a finite velocity of $\partial\xi^{(1)}/\partial t = -A\sin\theta$ in the x direction if the Atwood number is finite. Note also that Eq. (16) denotes an ellipse. The normalized circulation $\gamma = \Gamma/k$ is given as

$$\gamma^{(1)} = -2\cos\theta, \tag{17}$$

at this order. $\eta^{(1)}$, $\partial\eta^{(1)}/\partial\tau|_{\theta=0,\pi}$ in Eq. (16) and $\gamma^{(1)}$ in Eq. (17) coincide with the initial amplitude of the interface corrugation, the asymptotic linear growth rate and the initial circulation on the interface at $\tau = 0$, respectively.

Similar calculations yield at second order

$$\xi_2^{(2)} = \left[\frac{1-A^2}{4}\tau^2 + \frac{1-2A^2}{2}\alpha\tau\right]\sin 2\theta, \quad \xi_0^{(2)} = 0,$$

$$\eta_2^{(2)} = \frac{A\alpha\tau}{2}\cos 2\theta, \quad \eta_0^{(2)} = \frac{A\tau^2}{2} + \left(\frac{A\alpha}{2} + C\right)\tau, \tag{18}$$

where the superscript and subscript denote the order of ϵ and the mode number generated due to the nonlinear interaction, respectively. The integral constant C in Eq. (18) is determined to be $C = -A\alpha/2$ so that the initial velocity of $\eta_0^{(2)}$ is 0. Here we set $\xi_m^{(2)}(0) = \eta_m^{(2)}(0) = 0$ ($m = 0, 2$), i.e., we assume that the higher harmonics including the 0th mode do not exist initially. Note that the vertical component $\eta_0^{(2)}$ in Eq. (18) is derived from the mutual interaction between $\xi^{(1)}$ and $\eta^{(1)}$, which contributes to the difference of the growth between the bubble and spike as will be discussed in Secs. IV A and IV B. The circulation $\gamma^{(2)}$ is given as

$$\gamma^{(2)} = -A(\alpha + \tau)\cos 2\theta. \tag{19}$$

At third order, we have

$$\xi_3^{(3)} = \left[\frac{A\tau^3}{4}(1-A^2) + \frac{7A\alpha\tau^2}{8}(1-A^2)\right.$$
$$\left. + \frac{A\alpha^2\tau}{8}(11-12A^2)\right]\sin 3\theta,$$

$$\xi_1^{(3)} = \left[\frac{A\tau^3}{12}(5-3A^2) + \frac{A\alpha\tau^2}{8}(5-A^2)\right.$$
$$\left. + \frac{A\alpha^2\tau}{8}(3-8A^2)\right]\sin\theta,$$

$$\eta_3^{(3)} = \alpha^2\tau\left(A^2 - \frac{7}{8}\right)\cos 3\theta,$$

$$\eta_1^{(3)} = \left[\frac{\tau^3}{3}\left(A^2 - \frac{1}{2}\right) + \frac{\alpha\tau^2}{2}(-1+2A^2)\right.$$
$$\left. + \alpha^2\tau\left(A^2 - \frac{5}{8}\right)\right]\cos\theta, \tag{20}$$

$$\gamma_3^{(3)} = \left[-\frac{\tau^2}{2}\left(1 + \frac{7A^2}{3}\right) - \alpha\tau\left(1 + \frac{13A^2}{6}\right) - \alpha^2 A^2\right]\cos 3\theta,$$

$$\gamma_3^{(1)} = \left[-\frac{\tau^2}{2}(1+A^2) - \alpha\tau\left(1 - \frac{A^2}{2}\right) - \alpha^2 A^2\right]\cos\theta, \tag{21}$$

where we also set the initial condition that $\xi_m^{(3)}(0) = \eta_m^{(3)}(0) = 0$ ($m = 1, 3$).

By introducing the normalization time with the use of the asymptotic linear growth rate, i.e., $k v_{lin} t$, all of the physical variables are uniquely determined only with the Atwood number A and the initial corrugation amplitude of the interface α.

IV. DISCUSSIONS AND COMPARISON OF ANALYTICAL RESULTS WITH SIMULATIONS AND EXPERIMENTS

In this section, we use the same values of the parameters, such as the initial corrugation amplitude α and the Atwood number A, as those used in Sec. II otherwise specified to compare analytical results with simulations and experiments.

A. Nonlinear growth rate

First, we discuss the nonlinear growth rate of the bubble and spike. From Eqs. (16), (18), and (20), the velocities of bubble $\partial\eta_{bub}/\partial\tau$ and spike $\partial\eta_{spk}/\partial\tau$ are given within the third-order nonlinearity as

$$\frac{\partial\eta_{bub}}{\partial\tau} = \sum_{i=1}^{3} \frac{\partial\eta^{(i)}}{\partial\tau}\bigg|_{\theta=\pi}$$

$$= \left(-A^2 + \frac{1}{2}\right)\tau^2 + (-2A^2\alpha + A + \alpha)\tau$$

$$+ \left(-2A^2 + \frac{3}{2}\right)\alpha^2 + \frac{1}{2}A\alpha - 1,$$

$$\frac{\partial \eta_{spk}}{\partial \tau} = \sum_{i=1}^{3} \frac{\partial \eta^{(i)}}{\partial \tau}\Big|_{\theta=0}$$

$$= \left(A^2 - \frac{1}{2}\right)\tau^2 + (2A^2\alpha + A - \alpha)\tau$$

$$+ \left(2A^2 - \frac{3}{2}\right)\alpha^2 + \frac{1}{2}A\alpha + 1, \qquad (22)$$

where all modes appeared in each order are included in $\eta^{(i)}$. Equation (22) shows that the growth rates of the bubble and spike are not the same in the nonlinear regime as observed in the simulations. The nonlinear growth rate depends also on the initial amplitude of the interface corrugation, α, as shown in Eq. (22). It should be also noted that the proportionality of the linear growth rate to the initial corrugation amplitude has been included in the normalized time.

The difference between the simulation results and the analytical results in Fig. 2 can be improved by using the Padé approximants P_2^0 [17,18] given as

$$P_2^0\big|_{bub} = \frac{a_{bub}^3}{\left[a_{bub}\left(A^2 - \frac{1}{2}\right) + (-2A^2\alpha + A + \alpha)^2\right]\tau^2 - a_{bub}(-2A^2\alpha + A + \alpha)\tau + a_{bub}^2},$$

$$P_2^0\big|_{spk} = \frac{a_{spk}^3}{\left[-a_{spk}\left(A^2 - \frac{1}{2}\right) + (2A^2\alpha + A - \alpha)^2\right]\tau^2 - a_{spk}(2A^2\alpha + A - \alpha)\tau + a_{spk}^2},$$

where $P_2^0\big|_{bub}$ and $P_2^0\big|_{spk}$ denote the Padé approximants with respect to $\partial \eta_{bub}/\partial \tau$ and $\partial \eta_{spk}/\partial \tau$ in Eq. (22), respectively, and $a_{bub} = [(-2A^2 + 3/2)\alpha^2 + A\alpha/2 - 1]$ and $a_{spk} = [(2A^2 - 3/2)\alpha^2 + A\alpha/2 + 1]$. The coefficients are derived from Eq. (22).

The result using the Padé approximants P_2^0 is also shown in Fig. 2. We can see that the analytical results of the nonlinear growth rates agree quite well with the simulation results for relatively long time. All of the previous works that used the impulsive model had to introduce a free parameter to adjust the nonlinear growth rate. However, our model can uniquely determine the nonlinear evolution of the RM instability from the initial corrugation amplitude of the interface, the Atwood number of the interface before the incident shock hits, and the incident shock intensity.

We now compare our nonlinear prediction with experiments by Dimonte *et al.* in Ref. [19] where a rarefaction wave was reflected and the phase inversion of a interface occurs. Taking this fact into account [15], we evaluate the post shock variables such as the Atwood number $A = 0.584\,26$, the corrugation amplitude $\hat{\alpha}/\lambda = -2.0482/100$, and the linear growth rate $v_{lin} = 1.0542 \times 10^6$ cm/sec. (For details of the experiments, the reader is referred to Ref. [19], in which they showed that the transmitted shock detached the interface about 2.3 ns. Therefore we choose this time of the experiment as $t = 0+$ in our model.) In Fig. 4, we plot the bubble and spike amplitudes as functions of time and compare with the experimental points. It should be noted that in the experiments they did not resolve the bubble and spike separately but showed only Fourier mode amplitudes. Therefore, we also plot the amplitudes taken an average between the bubble and spike. In spite of the fact that the incident shock Mach number in the experiments is very high, $M = 15.3$, the analytical solutions agree fairly well with the experiment.

Figure 2 shows that as observed in the simulations, the analytical growth rate of the bubble decreases monotonously, while that of the spike increases once and has a peak at a certain time. This peak indicates that the velocity of the spike
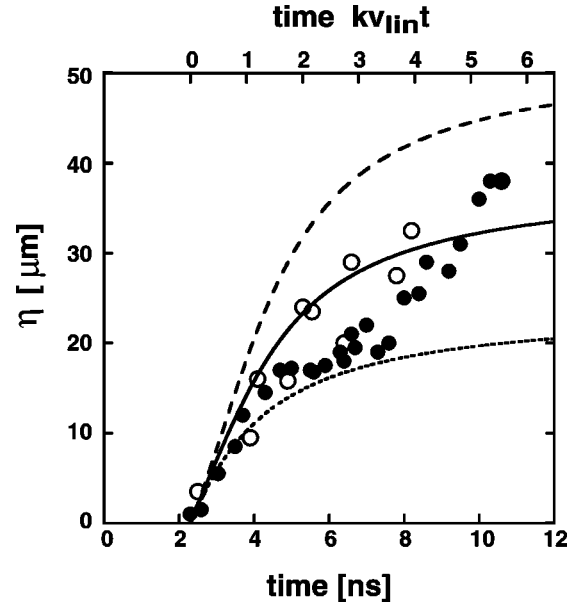

FIG. 4. Comparison of analytical nonlinear growth rate with the experiment [19]. Dashed and dotted lines depict bubble and spike amplitudes obtained using the Padé approximants, respectively, while the solid line depicts their average. Open and closed circles show experimental results in Fig. 15 in Ref. [19] with different methods of the measurement.
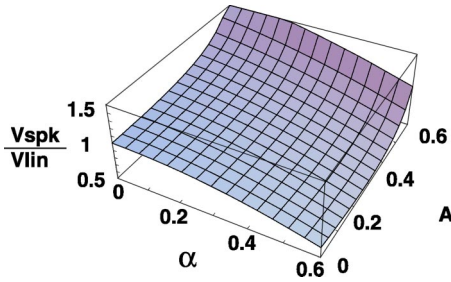
FIG. 5. Dependence of the maximum nonlinear growth rate of spike on Atwood number A and initial corrugation amplitude of interface α.

has an extremal value, which always exists for the case that $A \leq 1/\sqrt{2}$ within the third-order approximation as we see from $\partial \eta_{spk}/\partial \tau$ in Eq. (22). When the Atwood number is $A \geq 1/\sqrt{2}$, the velocity of the spike does not have the extremal value and the velocity diverges before time $\tau = 1$. This divergence is also found in the result of Velikovich and Dimonte [11] in which they assume that the Atwood number equals 1. Since Eq. (22) is a quadratic equation with respect to τ, we can calculate the maximum values of the nonlinear growth rate for the spike. We show the dependence of the maximum value of the spike growth rate on the Atwood number and the initial amplitude of the interface corrugation in Fig. 5. It is clearly seen that the larger Atwood number leads to the larger nonlinear growth rate, while the large amplitude of the initial corrugation decreases the maximum values of the nonlinear growth rate. The dependence of the nonlinear growth on the Atwood number will be also discussed in the following subsection.

B. Profile of bubble and spike

In our model, the interface is allowed to expand and contract in the tangential direction. We observe the motion of the Lagrangian markers in the simulations and compared it with the analytical results. We calculate the points of the Lagrangian markers by substituting Eqs. (16), (18), and (20) into the relation of $(x(\theta), y(\theta)) = (\theta + \Sigma_{i=1}^{3} \xi^{(i)}(\theta), \Sigma_{i=1}^{3} \eta^{(i)}(\theta))$. Figure 6 shows the simulation results of the shocked interface (left) and the vortex sheet (middle), and the analytical result (right). For the shocked interface at early time of τ

$= 0.05$, the displacement of the markers from the y axis (open circles in left figure) is relatively small compared with other two cases. This is due to the finite transition time required for the shocked interface to reach the asymptotic linear growth, as mentioned before. We show the motion of the Lagrangian markers with arrows. As is obvious from Fig. 6, the Lagrangian markers move in the x direction (horizontal direction) as well as in the y direction (vertical direction). The analytical results agree fairly well with the simulations.

The stretching of the interface can be calculated from $\partial s/\partial \tau$, where $s = \sqrt{[\theta + \xi(\theta)]^2 + \eta(\theta)^2}$. $\partial s/\partial \tau$ at $\tau = 0.8$ is shown in Fig. 7(a). At this time, the stretching of the interface in the spike is much larger than that in the bubble. It should be, however, noted that the maximum of the interface stretching appears not at the top of the spike but at the sides near the top. The double peaks of $\partial s/\partial \tau$ shown in Fig. 7(a) are due to the maximum stretching of the interface in the x direction in addition to the y direction as can be seen in Fig. 7 (b), which shows $\partial \xi/\partial \tau$. Namely, at this time the tip of the spike starts to expand in the x-direction to form the mushroom. It is noted that $\partial \xi/\partial \tau$ has both positive and negative values as shown in Fig. 7(b), which corresponds to the direction of the interface stretching (or shrinking) in the x coordinate as seen in the x component of the arrows shown in Fig. 6. In the regions where $\partial^2 \xi/\partial \tau \partial \theta < 0$, the interface is contracted in the x direction, while in the regions where $\partial^2 \xi/\partial \tau \partial \theta > 0$, the interface is expanding in the x direction.

In Fig. 8, we compare profiles of the interface obtained from our boundary conditions Eqs. (10) and (11), with those obtained from the boundary condition used by Zhang and Sohn [12], i.e., Eq. (13). It should be mentioned that Zhang and Sohn have expanded up to the fourth order, but we here use only up to the third order. We can see that the interface is strongly stretched in the tangential direction at the top of the spike in the case shown in Fig. 8(a) compared with that in the case shown in Fig. 8(b). Note that at time $\tau = 1$ in Fig. 8(b), the bubble structure is strongly deformed and the bubble curvature changes its sign, which is not observed in the simulation. The previous works [11,12] did not include the motion of the interface in the tangential direction, which may cause their failure to resolve the bubble structure at $\tau = 1$.
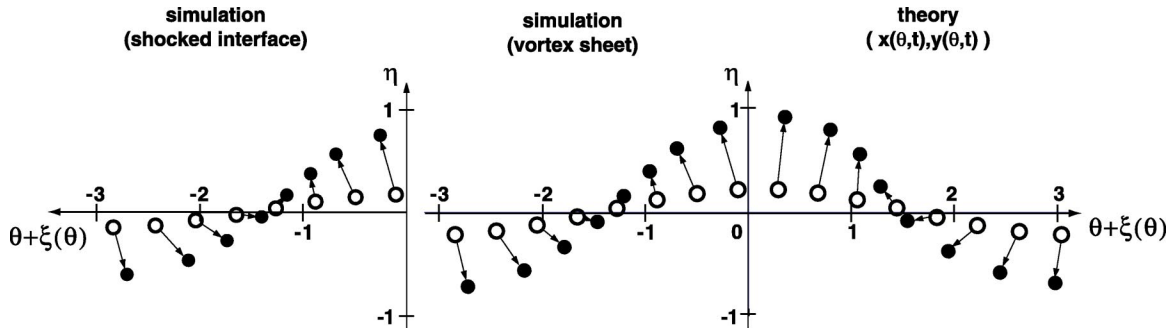

FIG. 6. Motion of the Lagrangian markers, where the horizontal axis is taken from $-\pi$ to 0 for the case of shocked interface (left), from $-\pi$ to 0 for the cases of vortex sheet (middle), and from 0 to π for analytical result (right). White and black circles depict positions of the Lagrangian markers at time of $\tau = 0.05$ and $\tau = 0.8$, respectively.

(a)

(b)

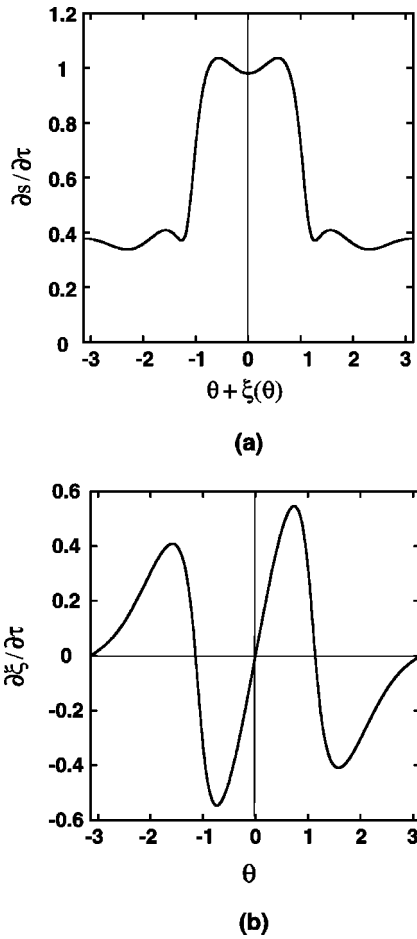FIG. 7. (a) Rate of change in dimensionless length of the interface, $\partial s/\partial\tau$ as a function of $\theta+\xi(\theta)$; and (b) deviation of the interface in the x direction, $\partial\xi/\partial\tau$ as a function of θ.

The boundary conditions, Eqs. (10)–(12), correspond to the following "modified" Birkhoff-Rott equation (it is often taken as $Z-Z'$ in the denominator in the integral instead of $Z'-Z$) [20,21]:

$$\frac{\partial Z^*}{\partial t} = \frac{1}{2\pi i}\int\frac{\kappa ds'}{Z'-Z} - \frac{A\kappa}{2}\frac{Z_\theta^*}{s_\theta},\qquad(23)$$

where $Z(t)=x+iy$, and $Z'(t)=x'+iy'$ denotes the position of the interface which is regarded as a vortex sheet, Z^* is the complex conjugate of Z and $\kappa ds = d\Gamma$ is the unit intensity of the vortex sheet with the line element ds related as $Z_\theta Z_\theta^* = s_\theta^2$. An analogous equation has been derived in Ref. [16] to investigate the motion of free surfaces. The second term on the right hand side of Eq. (23) gives rise to the interface motion in the tangential direction. Note that the second term is proportional to the Atwood number A and the vorticity κ. Since $\kappa=\nabla\Gamma$ changes its sign along the interface, the expansion and contraction of the interface occur locally in the tangential direction only for a finite Atwood number. We can easily check that the modified Birkhoff-Rott equation has the same solution as given by Eq. (16) by performing the complex integral of Eq. (23). The Birkhoff-Rott equation is ef-
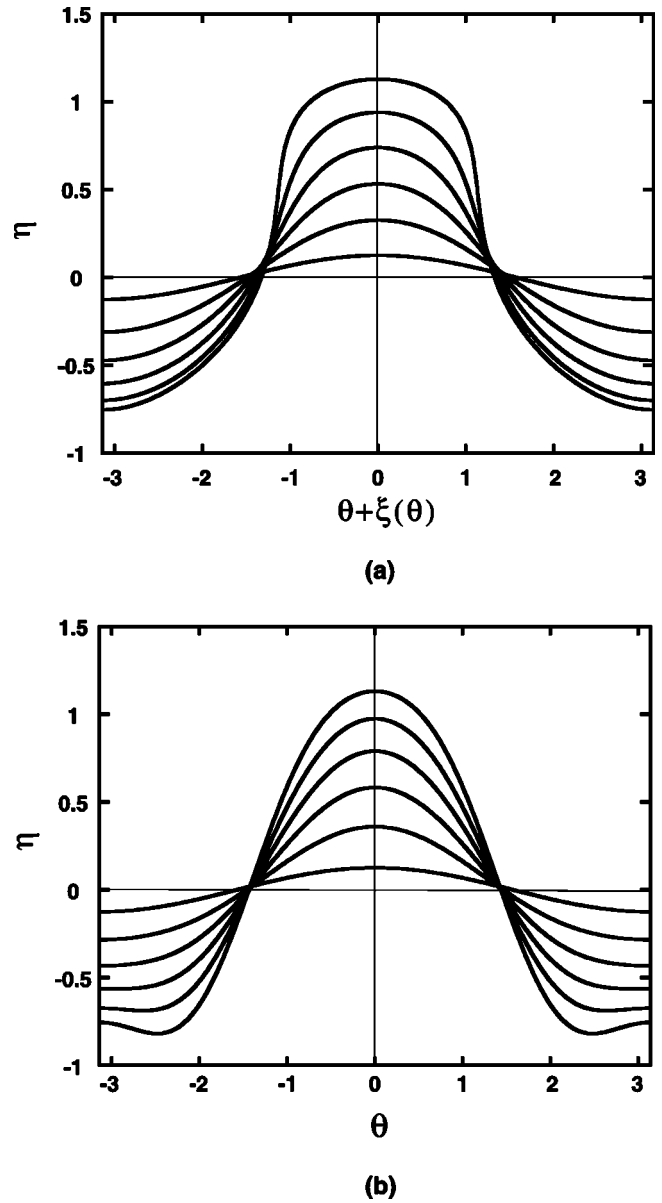

(a)

(b)

FIG. 8. Profiles of the interface with different boundary conditions: (a) given by Eqs. (10) and (11), $y=\eta$ against $x=\theta+\xi(\theta)$; and (b) given by Eq. (13), $y=\eta$ against $x=\theta$, where the initial corrugation amplitude of $\alpha=0.02\times2\pi$, the Atwood number of $A=0.376$; six lines are from near the $y=0$ axis at different times of $\tau=0, 0.2, 0.4, 0.6, 0.8, 1.0$, respectively.

fective to investigate the asymptotic behavior of the vortex sheet for large t. The analysis in terms of the Birkhoff-Rott equation will be published elsewhere.

We now discuss how the density jump affects the nonlinear growth and the profile of the bubble and the spike. In Fig. 9, we show the profiles of the interface with different Atwood numbers of (a) $A=0.2$, and (b) $A=0.6$ with the same initial corrugation amplitude of $\hat{\alpha}/\lambda=0.02$. It can be seen that the larger is the Atwood number, the faster is the nonlinear growth of the spike, while the slower is that of the bubble. This result indicates that in the nonlinear regime, if we consider a fixed mass density of the heavy fluid, as an
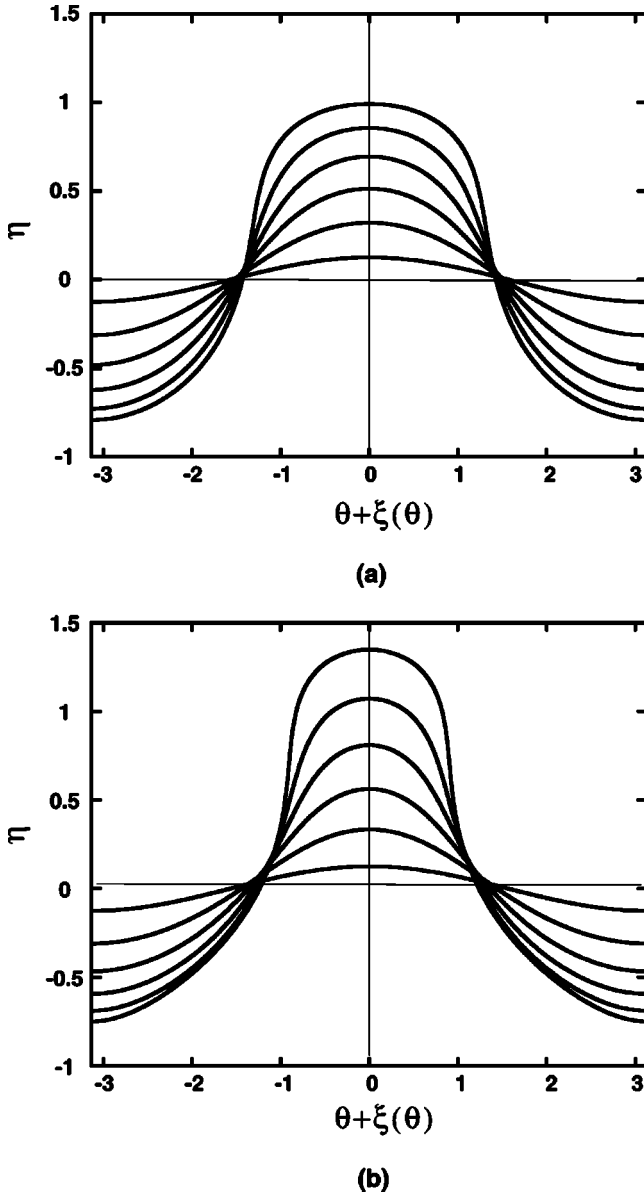
(a)

(b)

FIG. 9. Profiles of the interface with different Atwood numbers: (a) $A=0.2$ and (b) $A=0.6$, from near $y=0$ axis at $\tau=0$, 0.2, 0.4, 0.6, 0.8, and 1.0, respectively, where all parameters except the Atwood number are the same as Fig. 8.

example, the heavy material (spike) penetrates faster into the light fluid as the decrease of the light fluid mass density, while the light fluid (bubble) penetrates slower into the heavy fluid. It should be noted that the normalized time $\tau = k v_{lin} t$ includes the asymptotic linear growth rate that depends on the density ratio across the interface as given in Eq. (1). Therefore, this dependence of the growth on the Atwood number is not due to the dependence of the linear growth rate on the Atwood number, but due to the nonlinearity.

The profiles of the bubble and spike are symmetric in the linear theory, but not any more in the nonlinear regime. We see in Fig. 9, that the larger is the Atwood number, the narrower is the width of the spike, while the more flatten is the top of the bubble. This dependence of the nonlinear profiles of the bubble and the spike on the Atwood number is mostly
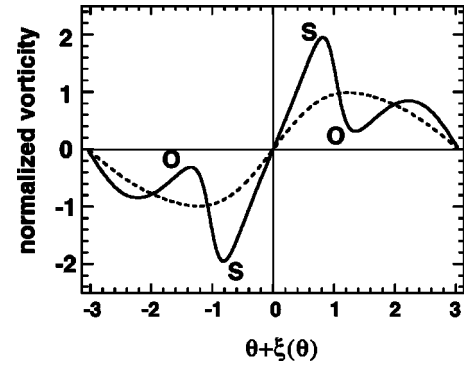

FIG. 10. Normalized vorticity $\nabla \gamma$ along the interface as a function of $\theta + \xi(\theta)$ at time $\tau=0.05$ (dashed line) and 0.8 (solid line).

due to the motion of the interface in the tangential direction, which is proportional to the Atwood number as shown in the second term in the right hand side of Eq. (23). Namely, as described before (in Fig. 6), the motion of the Lagrangian markers in the x direction increases with the increase of the Atwood number, which results in the narrow spike and the flatten bubble as the increase of the Atwood number.

C. Circulation and vorticity on interface

In the linear regime of the instability, the circulation on the interface does not change as given by Eq. (17) after the instability reaches the asymptotic linear growth rate. However, as shown in Eq. (5), the nonlinear terms drive the temporal evolution of the circulation along the interface with the finite Atwood number and thus generate higher harmonics of the circulation even if only a single mode exists initially. In a recent attempt [22] to apply a single-mode approximation to a two-fluid system in order to derive a heuristic drag model solution [23], the boundary conditions were not satisfied, which will be discussed in detail elsewhere. Figure 10 shows the vorticity distributions along the interface, $\kappa = d\gamma/ds = (x_\theta^2 + y_\theta^2)^{-1/2} d\gamma/d\theta$. They are calculated from Eqs. (17), (19), and (21). As a result of the continuous change of the vorticity on the interface, the vorticity distribution on the interface at $\tau=0.8$ becomes quite different from that at $\tau = 0.05$. Initially, there is only one mode. However, new local maxima and minima of the vorticity appear on the interface at $\tau=0.8$. The third harmonics of the vorticity leads mainly to these local maxima and minima.

The absolute values of the maximum and minimum vorticities at $\theta + \xi(\theta) \cong \mp 0.82$ ($\theta \cong \mp 0.80$) in Fig. 10 increase very rapidly with time, while those of the local maximum and minimum vorticities at $\theta + \xi(\theta) \cong \mp 1.38$ ($\theta \cong \mp 1.36$) in the same figure decrease further with the increase of time. We here call the former as point S, and the latter as point O, as indicated in the figure. It should be noted that the points, both S and O, change their position on the Lagrangian coordinate with time. Although the theory breaks up for large τ, we should mention the following facts observed in the simulation in which we can track the Lagrangian markers. Figure 11 shows some of the Lagrangian markers (dots) at $\tau=6$ and 12 corresponding to the density profiles shown in the right two figures in the bottom of Fig. 1. They were initially dis-
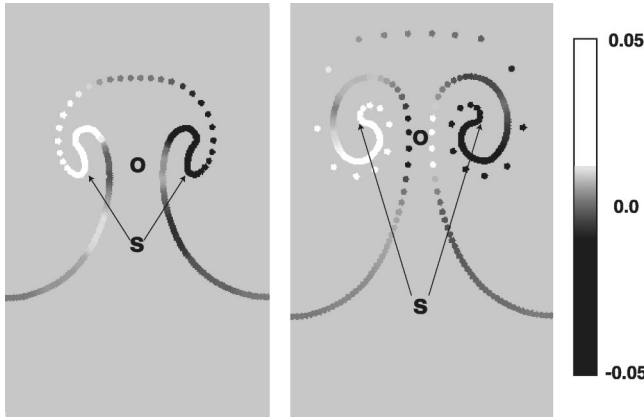
FIG. 11. Lagrangian markers for the case of the vortex sheet at time of $\tau=6$ (left) and 12 (right). They are initially distributed with equal distance between neighboring points. The gray scale of the dots indicates the z component of the vorticity, $\nabla\times\boldsymbol{v}$; white and black correspond to positive and negative values, respectively.

FIG. 12. Circulation on the interface: (a) temporal evolution of $\int_{\gamma>0}d\gamma$ (solid line) and average vorticity per unit interface length $\int_{\kappa>0}\kappa ds/\int ds$ (dashed line), both are normalized by their initial values; (b) dependence of $\int_{\gamma>0}d\gamma$ on the Atwood number A and the initial corrugation amplitude α at $\tau=0.8$, where $\int_{\gamma>0}d\gamma$ denotes the circulation $\int\kappa ds$ restricted to $\kappa>0$.

tributed with an equal distance between neighbor points along the interface, i.e., $\delta\theta=2\pi/N$, where $N=512$ is the number of the markers. Therefore different distances between neighbor Lagrangian markers in Fig. 11 indicate that the stretching and shrinking of the interface occurs locally. The stretching of the interface occurs mostly at the outer surface of the mushroom and at the joint between the mushroomumbrella and its stock. The shrinking of the interface occurs mostly at the inner surface of the mushroom spiral. We can also see other points where the interface is locally stretching or shrinking.

By observing the trajectories of the Lagrangian markers, we find that the point S in Fig. 10 turns out to be the tips of the spiral in the fully nonlinear phase of the instability as shown with S in Fig. 11. Namely, the maximum and minimum of the vorticity shown with S in Fig. 10 associate with the singularity that appears at the tips of the spiral in the system with the finite Atwood number. On the other hand, the point O in Fig. 10 moves to the joint of the mushroom umbrella and its stock as shown with O in Fig. 11. It should be noted that the points S and O in Fig. 10 correspond to the points near where the absolute value of $\partial\xi/\partial\tau$ has a maximum value and $\partial\xi/\partial\tau\simeq0$ at $\tau=0.8$, respectively, as seen in Fig. 7. Namely, at the point S, the interface starts to expand in the x direction at $\tau=0.8$, while the point O does not move much in the x direction after that time.

The gray scale of the dots in Fig. 11 indicates the z component of the vorticity, $\nabla\times v$, on the Lagrangian markers, which is calculated from the linear interpolation of the ones on its nearest four grid points in the simulation. Black and white correspond to negative and positive values of the z component of $\nabla\times v$, respectively, as scaled in the figure (arbitrary units). It should be noted that the sign of the z component of $\nabla\times v$ has the opposite sign of $\nabla\gamma$, defined in Sec. III. Since the initial vorticity $\nabla\gamma$ on the interface is negative in $\theta<0$, while that is positive in $\theta>0$, as shown with the dashed line ($\tau=0.05$) in Fig. 10, blight dots appear mostly in the left half of the interface ($\theta<0$), while dark dots appear mostly in the right half of the interface ($\theta>0$) as
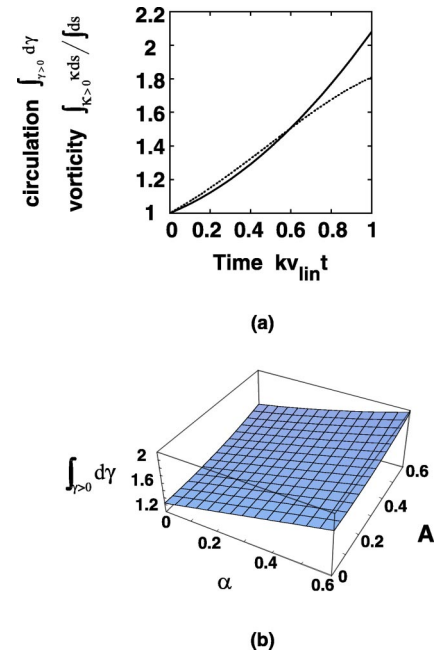
shown in Fig. 11(a) at $\tau=6$. However, we can see in Fig. 11(b) at $\tau=12$ that the points with a different darkness appear on the interface. We would like to emphasize that the different darkness appears near the point O in Fig. 11, i.e., black in the white (left), and vice versa (right), near the joint of the mushroom umbrella and its stock. Namely, in the strongly nonlinear regime of the instability, such as at $\tau=6$ and 12, the vorticity near the point O has an opposite sign from its initial value. It indicates that the decrease of the absolute value of the vorticity shown as O in Fig. 10 results in the opposite sign of the vorticity appearing at the joint. We would also like to mention that the appearance of the opposite sign of the vorticity near the point O may cause the generation of the double spiral structure of the mushroom in the RM instability, because the vorticity with the opposite sign induces the stretching of the interface in the tangential direction, as clearly seen from the comparison of the distances between the neighboring Lagrangian points near the point O at $\tau=6$ and with those at $\tau=12$ in Fig. 10.

Finally, we discuss the increase of the circulation on the interface with time and its dependence on the Atwood number A and the initial corrugation amplitude α in the RM instability. Since we assume initially a sinusoidal circulation, its integration along the interface over the wavelength becomes zero. Therefore, we calculate time evolution of $\int_{\gamma>0}d\gamma$ for only a region where $\gamma>0$ that denotes the circulation $\int\kappa ds$ restricted to $\kappa>0$, which is shown with solid line in Fig. 12(a). We can see the rapid increase of the circulation in the nonlinear regime of the instability. Since the total length of the interface increases also with time, the

increase of $\int_{\gamma>0} d\gamma$ does not always indicate the increase of the vorticity along the interface. Dashed line in Fig. 12(a) shows the average vorticity per unit length on the interface, $\int \kappa \, ds / \int ds$ for $\kappa > 0$. The values shown in the figure are normalized by their initial values. It is clearly seen that both the circulation and the average vorticity per unit length on the interface increase with time in the nonlinear phase of the RM instability. The increase of the circulation at early time is mainly due to the increase of the vorticity on the interface per unit length, while the increase at later time is mainly due the increase of the interface length.

In Fig. 12(b), we show the dependence of $\int_{\gamma>0} d\gamma$ on the Atwood number and the initial corrugation amplitude. Since $\int_{\gamma>0} d\gamma$ increases with time, the result shown in Fig. 12(b) is calculated at the normalized time $\tau = 0.8$. As clearly seen in the figure, the circulation increases faster with the increase of both the initial corrugation amplitude and the Atwood number. However, the increase of the circulation depends strongly on the initial corrugation amplitude α compared with the Atwood number A. This can explain the simulation result [13] showing that the larger is the initial corrugation amplitude, the faster is the speed of the roll up of the spiral at the tip of the mushroom. It is interesting to mention that the increase of the Atwood number accelerates the nonlinear growth rate of the spike and suppresses the nonlinear growth of the bubble as shown in the preceding section, while the increase of the initial corrugation amplitude enhances the increase of the circulation and thus accelerates the roll up motion of the spiral.

V. CONCLUSIONS

With the assumption of incompressible and irrotational fluids, we have developed an analytical model for a weakly nonlinear evolution of the RM instability. The theory shows that it is treated as a nonlinear self-interaction of a nonuniform vortex sheet with a density jump. With the proper kinematic boundary conditions, the Lagrangian description of the vortex sheet enables us to follow its nonlinear dynamics, such as its local stretching and shrinking in the tangential direction. By using the asymptotic linear growth rate of the RM instability, we have shown that the nonlinear evolution of the instability is uniquely determined from the initial corrugation amplitude of the interface, the Atwood number, and the incident shock intensity.

The theory reveals various nonlinear properties of the RM instability. For example, the increase of the Atwood number enhances the nonlinear growth of the spike, but reduces the nonlinear growth of the bubble. The larger is the Atwood number, the narrower is the width of the spike, while the more flatten is the top of the bubble. The density jump across the interface induces local increase and decrease of the vorticity on the interface. The larger is the initial corrugation amplitude, the larger is the nonlinear increase of the vorticity. The theory quantitatively gives those dependences on the Atwood number and the initial corrugation amplitude.

Although we have constructed the analytical model within a weak incident shock limit, the theory can be applicable even for a relatively large Mach number. The agreements of the analytical results with the simulations (Mach number of 2) and the experiments (Mach number of 15.3) show the validity of the model.

APPENDIX

In this appendix, we give a simple derivation of Eq. (5). Using relation (6), the Lagrange derivative of $\boldsymbol{u}_i$ ($i = 1,2$) is expressed by

$$\frac{D\boldsymbol{u}_i}{Dt} = \frac{\partial \boldsymbol{u}_i}{\partial t} + (\bar{\boldsymbol{u}} \cdot \boldsymbol{\nabla})\boldsymbol{u}_i = \frac{D_i \boldsymbol{u}_i}{Dt} + [(\bar{\boldsymbol{u}} - \boldsymbol{u}_i) \cdot \boldsymbol{\nabla}]\boldsymbol{u}_i, \quad \text{(A1)}$$

where

$$\frac{D_i}{Dt} = \frac{\partial}{\partial t} + \boldsymbol{u}_i \cdot \boldsymbol{\nabla}, \quad \boldsymbol{u}_1 = \boldsymbol{q} + \frac{\boldsymbol{\kappa}}{2}, \quad \boldsymbol{u}_2 = \boldsymbol{q} - \frac{\boldsymbol{\kappa}}{2}. \quad \text{(A2)}$$

Integrating Eq. (A2) along the sheet, we have for $\boldsymbol{u}_1$

$$\frac{D}{Dt} \int \boldsymbol{u}_1 \cdot ds = \int \frac{D_1 \boldsymbol{u}_1}{Dt} \cdot ds + \int \left[\left(\boldsymbol{q} - \frac{A\boldsymbol{\kappa}}{2} - \boldsymbol{u}_1 \right) \cdot \boldsymbol{\nabla} \right] \boldsymbol{u}_1 \cdot ds$$

$$+ \int \boldsymbol{u}_1 \cdot (ds \cdot \boldsymbol{\nabla}\bar{\boldsymbol{u}}), \quad \text{(A3)}$$

where we used the following relation:

$$\frac{D}{Dt} ds = d\frac{Ds}{Dt} = d\bar{\boldsymbol{u}} = ds \cdot \boldsymbol{\nabla}\bar{\boldsymbol{u}}$$

or the third term on the right-hand side of Eq. (A3). Here, ds is the line element vector along the sheet, d is identical to D on the sheet, and $\boldsymbol{\nabla}\bar{\boldsymbol{u}}$ denotes a tensor quantity such as $\partial \bar{u}_j / \partial x_k$. The second term on the right hand side of Eq. (A3) can be rewritten as

$$\int \left[\left(\boldsymbol{q} - \frac{A\boldsymbol{\kappa}}{2} - \boldsymbol{u}_1 \right) \cdot \boldsymbol{\nabla} \boldsymbol{u}_1 \right] \cdot ds$$

$$= \int (\boldsymbol{q} - \boldsymbol{u}_1) \cdot \boldsymbol{\nabla} \boldsymbol{u}_1 \cdot ds - \frac{A}{2} \int (\boldsymbol{\kappa} \cdot \boldsymbol{\nabla}) \boldsymbol{u}_1 \cdot ds. \quad \text{(A4)}$$

Returning to the third term on the right-hand side of Eq. (A3),

$$\int \boldsymbol{u}_1 \cdot (ds \cdot \boldsymbol{\nabla}\bar{\boldsymbol{u}}) = \int \boldsymbol{u}_1 \cdot (ds \cdot \boldsymbol{\nabla} \boldsymbol{q}) - \frac{A}{2} \int \boldsymbol{u}_1 \cdot (ds \cdot \boldsymbol{\nabla} \boldsymbol{\kappa}), \quad \text{(A5)}$$

in which

$$\int \boldsymbol{u}_1 \cdot (ds \cdot \boldsymbol{\nabla} \boldsymbol{\kappa}) = \frac{1}{2} \int \boldsymbol{\kappa} \cdot (ds \cdot \boldsymbol{\nabla} \boldsymbol{\kappa}) + \int \boldsymbol{q} \cdot (ds \cdot \boldsymbol{\nabla} \boldsymbol{\kappa}).$$
(A6)

If the gravity and the surface tension can be neglected, we have from Eqs. (A3)–(A6) that

$$\frac{D}{Dt} \int \boldsymbol{u}_1 \cdot ds$$

$$= -\frac{1}{\rho_1} \int \boldsymbol{\nabla} p \cdot ds - \frac{1}{4} \int (\boldsymbol{\kappa} \cdot \boldsymbol{\nabla}) \boldsymbol{\kappa} \cdot ds - \frac{1}{2} \int (\boldsymbol{\kappa} \cdot \boldsymbol{\nabla}) \boldsymbol{q} \cdot ds$$

$$- \frac{A}{2} \int (\boldsymbol{\kappa} \cdot \boldsymbol{\nabla}) \boldsymbol{q} \cdot ds - \frac{A}{4} \int (\boldsymbol{\kappa} \cdot \boldsymbol{\nabla}) \boldsymbol{\kappa} \cdot ds$$

$$+ \int \boldsymbol{q} \cdot \boldsymbol{\nabla} \boldsymbol{q} \cdot ds + \frac{1}{2} \int \boldsymbol{\kappa} \cdot ds \cdot \boldsymbol{\nabla} \boldsymbol{q}$$

$$- \frac{A}{4} \int \boldsymbol{\kappa} \cdot (ds \cdot \boldsymbol{\nabla} \boldsymbol{\kappa}) - \frac{A}{2} \int \boldsymbol{q} \cdot (ds \cdot \boldsymbol{\nabla} \boldsymbol{\kappa}),$$
(A7)

where we used the Euler equation

$$\frac{\partial \boldsymbol{u}_1}{\partial t} + (\boldsymbol{u}_1 \cdot \boldsymbol{\nabla}) \boldsymbol{u}_1 = -\frac{1}{\rho_1} \boldsymbol{\nabla} p.$$

Analogous calculations for $i = 2$ lead to

$$\frac{D}{Dt} \int \boldsymbol{u}_2 \cdot ds$$

$$= -\frac{1}{\rho_2} \int \boldsymbol{\nabla} p \cdot ds - \frac{1}{4} \int (\boldsymbol{\kappa} \cdot \boldsymbol{\nabla}) \boldsymbol{\kappa} \cdot ds + \frac{1}{2} \int (\boldsymbol{\kappa} \cdot \boldsymbol{\nabla}) \boldsymbol{q} \cdot ds$$

$$- \frac{A}{2} \int (\boldsymbol{\kappa} \cdot \boldsymbol{\nabla}) \boldsymbol{q} \cdot ds + \frac{A}{4} \int (\boldsymbol{\kappa} \cdot \boldsymbol{\nabla}) \boldsymbol{\kappa} \cdot ds + \int \boldsymbol{q} \cdot \boldsymbol{\nabla} \boldsymbol{q} \cdot ds$$

$$- \frac{1}{2} \int \boldsymbol{\kappa} \cdot ds \cdot \boldsymbol{\nabla} \boldsymbol{q} + \frac{A}{4} \int \boldsymbol{\kappa} \cdot (ds \cdot \boldsymbol{\nabla} \boldsymbol{\kappa})$$

$$- \frac{A}{2} \int \boldsymbol{q} \cdot (ds \cdot \boldsymbol{\nabla} \boldsymbol{\kappa}).$$
(A8)

Adding the third term and the seventh term in Eq. (A7) to

$$-\frac{1}{2} \int (\boldsymbol{\kappa} \cdot \boldsymbol{\nabla}) \boldsymbol{q} \cdot ds + \frac{1}{2} \int \boldsymbol{\kappa} \cdot ds \cdot \boldsymbol{\nabla} \boldsymbol{q}$$

$$= -\frac{1}{2} \int ds \cdot (\boldsymbol{\kappa} \cdot \boldsymbol{\nabla}) \boldsymbol{q} + \frac{1}{2} \int \boldsymbol{\kappa} \cdot ds \cdot \boldsymbol{\nabla} \boldsymbol{q}$$

$$= \frac{1}{2} \int (\boldsymbol{\kappa} \times ds) \cdot \boldsymbol{\nabla} \times \boldsymbol{q} = 0,$$
(A9)

where we used the relation

$$\boldsymbol{\nabla} \times \boldsymbol{q} = \frac{1}{2} \boldsymbol{\nabla} \times (\boldsymbol{u}_1 + \boldsymbol{u}_2) = 0,$$

which is obtained from the irrotationality $\boldsymbol{\nabla} \times \boldsymbol{u}_i = 0$ in each region i.

Taking into account Eq. (A9) and subtracting Eq. (A8) from Eq. (A7), we have

$$\frac{D}{Dt} \int \boldsymbol{u}_1 \cdot ds - \frac{D}{Dt} \int \boldsymbol{u}_2 \cdot ds$$

$$= -\frac{1}{\rho_1} \int \boldsymbol{\nabla} p \cdot ds + \frac{1}{\rho_2} \int \boldsymbol{\nabla} p \cdot ds - \frac{A}{2} \int (\boldsymbol{\kappa} \cdot \boldsymbol{\nabla}) \boldsymbol{\kappa} \cdot ds$$

$$- \frac{A}{2} \int \boldsymbol{\kappa} \cdot (ds \cdot \boldsymbol{\nabla}) \boldsymbol{\kappa}$$

$$= \left(\frac{1}{\rho_2} - \frac{1}{\rho_1} \right) \int \boldsymbol{\nabla} p \cdot ds - \frac{A}{2} \left[\int (\boldsymbol{\kappa} \cdot \boldsymbol{\nabla}) \boldsymbol{\kappa} \cdot ds \right.$$

$$\left. - \int \boldsymbol{\kappa} \cdot (ds \cdot \boldsymbol{\nabla}) \boldsymbol{\kappa} \right] - A \int \boldsymbol{\kappa} \cdot (ds \cdot \boldsymbol{\nabla}) \boldsymbol{\kappa}.$$
(A10)

The second term on the right-hand side of the last equality in Eq. (A10) leads to

$$-\frac{A}{2} \left[\int (\boldsymbol{\kappa} \cdot \boldsymbol{\nabla}) \boldsymbol{\kappa} \cdot ds - \int \boldsymbol{\kappa} \cdot (ds \cdot \boldsymbol{\nabla}) \boldsymbol{\kappa} \right]$$

$$= -\frac{A}{2} (\boldsymbol{\kappa} \times ds) \cdot \boldsymbol{\nabla} \times \boldsymbol{\kappa}$$

$$= (\boldsymbol{\kappa} \times ds) \cdot (\boldsymbol{\nabla} \times \bar{\boldsymbol{u}}) - (\boldsymbol{\kappa} \times ds) \cdot \boldsymbol{\nabla} \times \boldsymbol{q} = 0,$$

from which we have

$$\frac{D}{Dt} \int \boldsymbol{u}_1 \cdot ds - \frac{D}{Dt} \int \boldsymbol{u}_2 \cdot ds$$

$$= \frac{\rho_1 - \rho_2}{\rho_1 \rho_2} \int \boldsymbol{\nabla} p \cdot ds - A \int \boldsymbol{\kappa} \cdot (ds \cdot \boldsymbol{\nabla}) \boldsymbol{\kappa}$$

$$= \frac{\rho_1 - \rho_2}{\rho_1 \rho_2} p - \frac{A}{2} \boldsymbol{\kappa} \cdot \boldsymbol{\kappa}.$$
(A11)

Taking into account that the left-hand side of Eq. (A11) equals $D\Gamma/Dt$, we obtain

$$\frac{D\Gamma}{Dt} = \frac{\rho_1 - \rho_2}{\rho_1 \rho_2} p - \frac{A}{2} \boldsymbol{\kappa} \cdot \boldsymbol{\kappa}.$$
(A12)

Now adding Eqs. (A7) and (A8) to

$$\frac{D}{Dt} \int \boldsymbol{u}_1 \cdot ds + \frac{D}{Dt} \int \boldsymbol{u}_2 \cdot ds$$

$$= 2 \frac{D\Phi}{Dt}$$

$$= -\frac{\rho_1 + \rho_2}{\rho_1 \rho_2} p - \frac{1}{4} \boldsymbol{\kappa} \cdot \boldsymbol{\kappa} + \boldsymbol{q} \cdot \boldsymbol{q} - A \boldsymbol{\kappa} \cdot \boldsymbol{q}.$$
(A13)

By deleting the pressure p from Eqs. (A12) and (A13), we obtain Eq. (5):

$$\frac{D\Gamma}{Dt} = 2A\left[\frac{D\Phi}{Dt} - \frac{1}{2}\mathbf{q}\cdot\mathbf{q} - \frac{1}{8}\boldsymbol{\kappa}\cdot\boldsymbol{\kappa} + \frac{A}{2}\boldsymbol{\kappa}\cdot\mathbf{q}\right]_{\text{interface}}.$$

Note that if we set $A = 0$ in this equation, the well-known

Kelvin's circulation theorem $D\Gamma/Dt = 0$ is obtained. We add that Eq. (5) equals to the Bernoulli equation

$$\rho_1\left[\frac{\partial\phi_1}{\partial t} + \frac{1}{2}(\boldsymbol{\nabla}\phi_1)^2\right] = \rho_2\left[\frac{\partial\phi_2}{\partial t} + \frac{1}{2}(\boldsymbol{\nabla}\phi_2)^2\right],$$

taking into account the relation $\Gamma = \phi_1 - \phi_2$.

---

[1] R.D. Richtmyer, Commun. Pure Appl. Math. **13**, 297 (1960).

[2] Y. Yang, Q. Zang, and D.H. Sharp, Phys. Fluids **6**, 1856 (1994).

[3] J.W. Jacobs and J.M. Sheeley, Phys. Fluids **8**, 405 (1996).

[4] A.L. Velikovich, Phys. Fluids **8**, 1666 (1996).

[5] M.A. Jones and J.W. Jacobs, Phys. Fluids **9**, 3078 (1997).

[6] J.G. Wouchuk and K. Nishihara, Phys. Plasmas **3**, 3761 (1996).

[7] J.G. Wouchuk and K. Nishihara, Phys. Plasmas **4**, 3761 (1997).

[8] K. Nishihara, R. Ishizaki, J.G. Wouchuk, Y. Fukuda, and Y. Shimuta, Phys. Plasmas **5**, 1945 (1998).

[9] N.J. Zabusky, Annu. Rev. Fluid Mech. **31**, 495 (1999).

[10] A. Rikanati, U. Alon, and D. Shvartz, Phys. Rev. E **58**, 7410 (1998), and references therein.

[11] A.L. Velikovich and G. Dimonte, Phys. Rev. Lett. **76**, 3112 (1996).

[12] Q. Zhang and S. Sohn, Phys. Fluids **9**, 1106 (1997).

[13] K. Nishihara, Y. Fukuda, C. Matsuoka, and J.G. Wouchuk, in *Proceedings of the Seventh International Workshop on Physics of Compressible Turbulent Mixing, St. Petersburg 1999*, edited by E. Meshkov, Yu. Yanilkin, and V. Zhmalio (RFNC-VNIIEF, Sarov, Russia, 2001), p. 320.

[14] H. Sakagami and K. Nishihara, Phys. Fluids **2**, 2715 (1990).

[15] J.G. Wouchuk, Phys. Plasmas **8**, 2890 (2001).

[16] G.R. Baker, D.I. Meiron, and S.A. Orszag, J. Fluid Mech. **123**, 477 (1982).

[17] G.A. Baker and P. Graves-Morris, *Padé Approximants* (Addison-Wesley, Reading, MA, 1981).

[18] Q. Zhang and S. Sohn, Phys. Lett. A **212**, 149 (1996).

[19] G. Dimonte, C.E. Frerking, M. Schneider, and B. Remington, Phys. Plasmas **3**, 614 (1996).

[20] G. Birkhoff, in *Proceedings of Symposium in Applied Mathematics* (American Mathematical Society, Providence, 1962), Vol. XIII.

[21] N. Rott, J. Fluid Mech. **1**, 111 (1956).

[22] V.N. Goncharov, Phys. Rev. Lett. **88**, 134502 (2002).

[23] U. Alon, J. Hecht, D. Offer, and D. Shavarts, Phys. Rev. Lett. **74**, 534 (1995).